RSC Advances

ROYAL SOCIETY OF CHEMISTRY

PAPER

View Article Online
View Journal | View Issue

Check for updates

Cite this: *RSC Adv.*, 2026, **16**, 21381

Research on the regulation of osteogenic differentiation and mechanotransduction by porous bionic coatings on titanium alloy implant surfaces

Zhuan Zou,†[b] Shuhan Jiang,†[a] Wenjin Chen,†[c] Yilong Wang,[a] Qu Liang,[d] Wei Fang,[d] Xinli Zhan,*[b] Ronghe Gu *[d] and Quanzhi Chen*[ae]

To elucidate the mechanism underlying micro-arc oxidation (MAO) coatings in bone regeneration, biomimetic coatings with different surface roughness were fabricated on titanium alloy substrates *via* MAO, and their effects on osteogenic differentiation and mechanotransductive signaling were investigated. The prepared hydroxyapatite (HA)-containing MAO coating exhibited a porous micro-nano structure, with porosity and micro-roughness ranging from 28.1% to 38.6% and 9.3 to 15.8 μm, respectively. Cell experiments demonstrated that the coating with a porosity of 35.6% and a roughness of 15.8 μm significantly promoted cell adhesion, proliferation, and osteogenic differentiation (with a 76.0% increase in alkaline phosphatase activity relative to the NC group), while upregulating the expression of downstream target genes YAP1, Runx2 and OCN. Micro-CT results revealed that the 500 V coating group exhibited a 30.9% increase in bone volume fraction and an 81.3% elevation in trabecular thickness relative to the NC group, with the bone-implant contact ratio showing a corresponding 44.6% enhancement. Histological analysis further confirmed that the elevated porosity and surface roughness facilitated the tight encapsulation of the porous coating structure by newly formed bone tissue. Bond strength testing revealed that the 500 V coating group achieved an interfacial bond strength of 33.2 N after 42 days *in vivo*, representing a 55.87% increase compared with the NC group. This study elucidated the influence of surface roughness on osseointegration, providing a theoretical basis for optimising the surface microstructure of implant materials.

Received 10th February 2026
Accepted 10th April 2026

DOI: 10.1039/d6ra01182a

rsc.li/rsc-advances

1 Introduction

Within the organism, cells inhabit a sophisticated microenvironment comprising the extracellular matrix (ECM), adjacent cells, and bodily fluids.[1,2] The intricate cellular niche precisely modulates cell proliferation, differentiation and functional expression through diverse biophysical and biochemical signals, and decisively modulates cell behavior *via* mechanosensing and chemical signal transduction pathways.[3,4] During bone injury repair, bone marrow mesenchymal stem cells (BMSCs) initially adhere to implant surface, undergo pivotal biological processes including proliferation and lineage-specific differentiation, and ultimately generate new bone tissue.[5] This cascade of cellular events is highly dependent on the local microenvironment formed by the compositional and micro/nano-structural features of implant materials. The physicochemical properties of material surfaces have been proven to directly regulate stem cell fate determination and osteogenic differentiation efficiency.[6,7] Consequently, the precise design and modulation of implant microenvironmental properties, including surface topography, mechanical properties, and the spatial distribution of bioactive molecules, have emerged as a research frontier in bone tissue engineering and regenerative medicine.

Micro-arc oxidation (MAO) technology enables the *in situ* fabrication of TiO_2-dominated micro/nano composite ceramic coatings on titanium alloy surfaces, holding substantial promise for orthopedic implant applications.[8] Such coatings feature a three-dimensional interconnected porous network featuring coexisting micrometer-scale primary pores and

---

[a] *School of Basic Medical Sciences, Guangxi Medical University, Nanning 530021, Guangxi, P. R. China. E-mail: quanzhi_chen@163.com*

[b] *Department of Spine and Osteopathic Surgery, The First Affiliated Hospital of Guangxi Medical University, Nanning 530021, Guangxi, P. R. China. E-mail: zhanxinli@stu.gxmu.edu.cn*

[c] *Pediatric Dentistry Department, College & Hospital of Stomatology, Guangxi Medical University, Nanning 530021, Guangxi, P. R. China*

[d] *Department of Spine Surgery, The Fifth Affiliated Hospital of Guangxi Medical University, Nanning 530021, Guangxi, P. R. China. E-mail: nnsygrh@sr.gxmu.edu.cn*

[e] *University Engineering Research Center of Advanced Technologies in Medical and Biological Intelligent Manufacturing, Guangxi Medical University, Nanning 530021, Guangxi, P. R. China*

† These authors contributed equally to this work.

nanoscale secondary structures, which biomimetically recapitulate the physical niche of the native bone extracellular matrix.[9,10] Previous studies reported that MAO coatings with a biomimetic trabecular topology with 65% porosity and ~600 μm equivalent pore size more effectively promoted osteoblast adhesion, proliferation and differentiation.[11,12] Experiments using beagle mandibular implants further revealed that the MAO coating exhibited significantly enhanced peri-implant new bone formation, higher bone-implant contact (BIC) rates, and tighter interface bonding.[13,14] This coating architecture also provides a foundational strategy for the structure-function synergistic optimization in bone defect repair.[15,16] The porous structure enlarges the specific surface area, facilitating the adsorption and conformational unfolding of adhesion proteins such as fibronectin, promoting nutrient and metabolite transport, and providing stable anchoring for cells, thereby significantly enhancing the adhesion, spreading, proliferation and osteogenic differentiation of BMSCs.[17–19] Furthermore, improving coating hydrophilicity,[20] adjusting surface charges, or regulating the chemical microenvironment *via* doping with osteogenic ions (such as Ca, P, Sr) or loading bioactive agents (*e.g.*, BMP-2, antibiotics) can synergistically boost coating bioactivity and anti-infective performance.[21,22] These modifications guided MC3T3-E1 cells to form elongated pseudopodia, acquire a well-spread morphology, and develop dense stress fibers, optimizing mechanical coupling between cells and the scaffold and laying a structural basis for osteogenic signaling activation.[23–25] However, current research remains largely confined to the "structure-phenotype" correlation level, and few systematic studies have elucidated the mechanisms underlying osteogenic differentiation by exploring how the local microenvironment (encompassing coating composition and topography) modulates cellular mechanosensitivity.

Biomechanical cues serve as key regulators of cell fate specification and have garnered increasing attention.[26] In addition, mechanical stress can regulate cellular behavior by activating mechanical transduction signaling cascades. Among these, YAP1 (Yes-associated protein 1), the core effector of the Hippo pathway, undergoes dynamic nucleocytoplasmic shuttling in response to varying mechanical stimuli.[27] Specifically, nuclear YAP1/TAZ acts as a transcriptional co-activator to drive the expression of downstream target genes, thereby governing cell proliferation, differentiation, survival, and migration, and plays an essential role in regulating osteogenic differentiation.[28] Studies have demonstrated that rough surfaces, patterned structures, and fibrous substrates can significantly enhance osteogenic differentiation by promoting nuclear translocation and activation of YAP/TAZ.[29] For instance, optimal YAP/TAZ activation and osteogenesis were achieved on hydroxyapatite disks with a surface roughness of 0.77–1.09 μm and a peak distance of 39.3–53.9 μm.[30] Similarly, grid-like PDMS micropatterns enhanced YAP activation and osteogenic differentiation in MC3T3-E1 preosteoblasts.[31] Specific nanopatterns (70 nm and 200 nm) have also been shown to promote osteogenesis *via* TAZ activation in human mesenchymal stem cells.[32] However, the molecular mechanisms by which the surface characteristics of micro-arc oxidation (MAO) coatings regulate bone regeneration *via* mechanotransduction pathways remain poorly understood.

In this study, biomimetic porous coatings with gradient roughness were fabricated on titanium alloy surfaces *via* MAO technology, and the regulatory effects of surface architecture on BMSCs adhesion, spreading, proliferation, and osteogenic differentiation were systematically explored. We employed a multiscale analysis that integrated *in vitro* cellular mechanoresponses (proliferation, F-actin cytoskeletal remodeling, and YAP1 nuclear translocation) with *in vivo* osseointegration efficiency, to provide an in-depth analysis of the molecular mechanisms underlying the MAO coating structure and osteogenic differentiation. This study would provide a theoretical basis for promoting MAO modification of titanium alloy implant surfaces.

2 Materials and methods

2.1 Coating preparation and characterisation

This study employed medical-grade titanium alloy (TA2, purity ≥99.5%, dimensions 10 mm × 10 mm × 2 mm) as the substrate material. The substrate was pretreated *via* the following steps: sequential polishing with waterproof abrasive paper from 500# to 1200# grit, ultrasonic cleaning in acetone for 15 min to remove organic contaminants, ultrasonic cleaning in deionized water for 10 min, ultrasonic cleaning in ethanol for 10 min, and final air-drying at room temperature for subsequent use.

2.1.1 Coating preparation. Custom micro-arc oxidation equipment was used in this study. Biomimetic coatings were fabricated on the substrates *via* constant current-mode MAO technology, with an alkaline aqueous electrolyte solution containing 10 g L^{-1} $Ca(CH_3COO)_2\cdot H_2O$ and 8 g L^{-1} $NaH_2PO_4\cdot 12H_2O$, 20 g L^{-1} Na_2SiO_3, 4 g L^{-1} KF^{-1}, and 2 g L^{-1} NaOH employed for coating preparation. The electrical parameters were set as follows: a frequency of 500 Hz, a constant current density of 2 A dm^{-2}, and a duty cycle of 15%. Three sample groups with gradient surface roughness were prepared by adjusting the oxidation termination voltage to 400 V, 450 V, and 500 V, respectively. During the entire preparation process, the electrolyte temperature was strictly maintained at 25 ± 2 °C using a circulating cooling system. After MAO treatment, the samples were thoroughly rinsed with deionized water and air-dried at room temperature. For a comprehensive evaluation of the *in vitro* and *in vivo* bone regenerative potential of the biomimetic coatings, polished titanium alloy substrates without MAO treatment were designated as the normal control (NC) group.

2.1.2 Surface roughness analysis. The surface roughness of MAO coating was determined *via* atomic force microscopy (AFM, Hitachi 5100 N, Japan), with subsequent analysis performed using the device's native software. The testing area for each coating roughness measurement was set to 30 μm × 30 μm.

2.1.3 Morphological analysis. The surface microstructure of MAO coating was observed using field-emission scanning electron microscope (SEM, Hitachi SU-8010, Japan), and operated at an accelerating voltage of 10 kV. The elemental distribution of the coatings was characterized by energy-dispersive X-ray spectroscopy (EDS) attached to the SEM. Coating porosity was quantified from on SEM images using Image J software, with 10 randomly selected fields of view per sample group for statistical assessment.

2.1.4 Phase structure analysis. The phase structure of the MAO coating was identiffed using X-ray diffraction (XRD) on a PANalytical X'Pert PRO instrument equipped with Cu Kα radiation. XRD measurements were performed with a step size of 0.026°, an incident angle of 10°, operating voltage 40 kV, operating current 30 mA, and scanning range $2\theta = 10°–80°$. The XRD patterns were analysed using X'Pert HighScore software to identify the crystalline phases.

2.1.5 Surface wettability analysis. A contact angle goniometer (Dataphysics OCA20, Germany) was used to measure the water contact angle of the coating surfaces at room temperature. A 5 μL deionized water droplet was dropped onto the sample surface, and the contact angle was recorded after the droplet stabilized (~5 s). Three distinct non-overlapping positions were tested per sample, and the average value was calculated for statistical analysis.

2.1.6 X-ray photoelectron spectroscopy (XPS). The chemical bonding states of Ca, P, O, and Ti elements in the MAO coatings were characterized by XPS (Thermo Fisher Scientific K-Alpha, USA) with Al Kα radiation. The test spot size was 400 μm, and the obtained spectra were calibrated with the C 1s peak (284.8 eV) for charge correction. The high-resolution spectra of Ca 2p, P 2p, and O 1s were fitted and analysed using XPS Peak Fit software.

2.2 Cell experiments

2.2.1 Cell isolation and culture. To evaluate the impact of coating structures on osteogenic differentiation potential, BMSCs were co-cultured with MAO coatings. The BMSCs were provided by the Endodontic Laboratory at the School of Stomatology, Guangxi Medical University. These cells were isolated from the bone marrow of the femoral head of Sprague-Dawley (SD) rats and subjected to primary culture. Flow cytometry analysis following passage to the third generation confirmed the expression of markers including CD34, CD45, CD44, and CD29, with a stem cell purity of over 90%. The cells were cultured in Dulbecco's Modiffed Eagle Medium (DMEM, Gibco™) supplemented with 10% fetal bovine serum (FBS) and an antibiotic mixture (100 U/mL penicillin and 0.1 mg mL^{-1} streptomycin sulfate, Sigma-Aldrich). Cells were placed in an incubator (PHCbi MCO-18AIC) and cultured at 37 °C with 5% CO_2. The cells were passaged to the third generation and used for subsequent experiments.

2.2.2 Experimental grouping. The experiment was divided into 4 groups: NC group, 400 V MAO coating, 450 V MAO coating, and 500 V MAO coating group. All cell experiments were performed in triplicate, and each replicate was repeated 3 times independently.

For cytotoxicity analysis, the third-generation BMSCs (1.0×10^4 cells per well) were seeded onto the coating surfaces, which were then placed in 24-well plates. Co-cultured for 48 h, the medium was carefully removed, and the cells were stained with the Live/Dead staining kit (Invitrogen, USA) for 15 min under light-protected conditions. Finally, a fluorescence microscope (Zeiss, Germany) was utilized to observe and document the samples.

For cell proliferation assays, third-generation BMSCs were inoculated onto the different coating surfaces in a 24-well plate at a density of 1.0×10^4 cells per well. The cells were then incubated in a cell incubator for 1, 3, and 5 days, respectively. After each incubation period, the culture medium was carefully aspirated and discarded. The wells were washed three times with PBS, after which 500 μL of complete culture medium supplemented with 10% CCK-8 solution (NCM Bio, Suzhou, China) was added to each well. The 24-well plate was placed back into the incubator for 4 h to ensure complete reaction stability. Subsequently, 200 μL of the reaction solution from each well was transferred to a 96-well plate, and the absorbance values at a wavelength of 450 nm were measured using an enzyme-labeled instrument (Biotek, USA).

For cytoskeleton observation, samples were placed in a 24-well plate, and BMSCs were seeded onto the coating surface at an density of 1×10^4 cells/well. After 48 h of co-culture, the cells were washed with PBS and fixed using 4% paraformalde. Cells were osmotically stabilised by treatment with 0.2% Triton X-100 in PBS for 5 min, then incubated in the dark at 4 °C for 12 h with an appropriate volume of rhodamine-labeled phalloidin (5 units per mL) diluted in PBS. After rinsing with PBS, cell nuclei were stained with Hoechst 33 258 at 4 °C for 10 min. Following a final wash with PBS, the cells were observed and imaged using a fluorescence microscope (Zeiss, Germany).

2.2.3 Alkaline phosphatase (ALP) and YAP1 activity detection. The third-generation BMSCs were seeded onto the coating surfaces (6-well plates) at a density of 5.0×10^4 cells per well and co-cultured for 14 days (the culture medium was replaced every 2 days). At the end of the culture, the cells were rinsed twice with PBS, digested with 0.25% trypsin–EDTA (Gibco™, USA) for 3 min, and centrifuged at $1000 \times g$ for 5 min to collect the cell pellet. The cell pellet was resuspended in RIPA lysis buffer (Beyotime, China) containing 1% phenylmethylsulfonyl fluoride (PMSF, Beyotime, China) and lysed on ice for 30 min, then centrifuged at $12\,000 \times g$ for 15 min at 4 °C to collect the supernatant. The protein concentration of the cell lysate was determined using a BCA Protein Assay Kit (Beyotime, China). The activities of ALP and YAP1 were detected using rat ALP ELISA Kit and rat YAP1 ELISA Kit (both from Beyotim, China) according to the kit instructions. The absorbance value at 405 nm was measured using a microplate reader, and the activity levels of ALP and YAP1 were calculated based on the standard curves, normalized to the total protein concentration of the cell lysate.

2.2.4 Osteogenic-related gene expression analysis. The third-generation BMSCs were seeded onto the coating surfaces (6-well plates) at a density of 5.0×10^4 cells per well and co-cultured for 14 days. Total RNA was extracted from the cells using TRIzol reagent (Invitrogen, USA, Cat. No. 15596-026) according to the manufacturer's instructions: 1 mL TRIzol was added to each well, and the cells were lysed by pipetting repeatedly, followed by sonication for 30 s (power 300 W, work 3 s, interval 5 s) to ensure complete cell lysis. Then 0.2 mL chloroform was added to each 1 mL TRIzol lysate, shaken vigorously for 15 s, and incubated at room temperature for 3 min, then centrifuged at 12 000×*g* for 15 min at 4 °C. The upper aqueous phase was transferred to a new centrifuge tube, and an equal volume of isopropanol was added, mixed gently, and incubated at room temperature for 10 min, then centrifuged at 12 000×*g* for 10 min at 4 °C to precipitate RNA. The RNA pellet was washed twice with 75% ethanol (prepared with DEPC water), centrifuged at 7500×*g* for 5 min at 4 °C, air-dried at room temperature for 5–10 min, and dissolved in 20 μL RNase-free water. The concentration and purity of total RNA were determined using a NanoDrop 2000 spectrophotometer (Thermo Fisher Scientific, USA).

Reverse transcription was performed using 1 μg of total RNA with the All-in-One qRT Master Mix II (Yunbio, China), which included a genomic DNA elimination step. The reaction system (20 μL total volume) consisted of 1 μg total RNA, 5 μL of 5× gDNA Eliminator Buffer, 2 μL of 5× PrimeScript Buffer, 1 μL of PrimeScript RT Enzyme Mix, and nuclease-free water. The thermal cycling conditions were: 37 °C for 15 min for reverse transcription, 85 °C for 5 s for enzyme inactivation, and held at 4 °C. The resulting cDNA was diluted 10-fold with nuclease-free water prior to qPCR amplification.

qPCR was carried out on ABI 7500 system using 2×Q3 SYBR qPCR Master Mix(Universal). The specific primer sequences for Runx2, OCN, and the reference gene GAPDH are listed in Table 1. The thermal cycling protocol involved an initial denaturation at 95 °C for 30 s, followed by 40 cycles of 95 °C for 5 s and 60 °C for 30 s. Melting curve analysis was performed to verify primer specificity. Relative gene expression was calculated using the $2^{-\Delta\Delta Ct}$ method, with GAPDH as the internal control. The expression level in the NC group was normalized to 1.0. All experiments were performed in triplicate.

2.3 *In vivo* experiments

2.3.1 Experimental animals and grouping. A total of 48 healthy male SD rats (8 weeks-old, SPF grade, body weight 250 ± 20 g, provided by the Experimental Animal Center of Guangxi Medical University) were randomly divided into four groups ($n = 12$ per group): NC group, 400 V MAO coating group, 450 V MAO coating group, and 500 V MAO coating group. The animals were raised with free access to food and water. All animal experiments were approved by the Animal Ethics Committee of Guangxi Medical University and performed in accordance with the National Institutes of Health (NIH) Guide for the Care and Use of Laboratory Animals.

Table 1 Primer sequences for qPCR detection of osteogenesis-related genes

Target gene	Primer sequence (5′–3′)
Runx2-forward primer	CAACTTCCTGTGCTCCGTGC
Runx2-reverse primer	CATGACGGTAACCACGGTCC
OCN-forward primer	AGGACCCTCTCTCTGCTCACT
OCN-reverse primer	CTATTCACCACCTTACTGCCC
GAPDH-forward primer	CAAGATGGTGAAGGTCGGTG
GAPDH-reverse primer	TGCCGTGGGTAGAGTCATACTG

2.3.2 Femoral bone defect model establishment and implant implantation. Rats were anesthetized by intraperitoneal injection of 10% chloral hydrate (300 mg kg^{-1} body weight). After anesthesia, the right hind limb was shaved and disinfected with 75% ethanol and 5% iodophor successively. A 3 cm longitudinal incision was made at the proximal femur of the right hind limb, the skin and subcutaneous tissue were separated layer by layer, and the femoral shaft was exposed by blunt separation of the muscle. A cylindrical bone defect with a diameter of 1.5 mm and a depth of 2 mm was created on the femoral shaft using a sterile Kirschner wire (diameter 1.5 mm) with a dental drill. The sterile implant samples ($\varphi = 1.5$ mm, $h = 2$ mm, sterilized by high-pressure steam at 121 °C for 30 min) were implanted into the bone defects to ensure tight contact between the implant and the host bone. The muscle, subcutaneous tissue, and skin were sutured layer by layer with absorbable sutures. Postoperatively, penicillin (80 000 U per kg) was intramuscularly injected once a day for 3 consecutive days to prevent infection, and the wound healing was monitored daily.

2.3.3 Sample collection. The rats were sacrificed by cervical dislocation at 2, 4, and 6 weeks post-implantation ($n = 3$ per group at each time point).

(1) At each time point, the right femur with the implant was harvested, the soft tissue was removed carefully, and part of the samples were used for micro-CT scanning and push-out mechanical testing.

(2) At 4 weeks post-implantation, an additional 3 rats per group were sacrificed to harvest the liver tissue (for biosecurity evaluation) and the femoral implant samples (for histological and immunohistochemical analysis).

2.3.4 Micro-CT analysis. Bone regeneration at the defect site was assessed *via* micro-CT at 2, 4, and 6 weeks post-surgery. The harvested bone specimens were subjected to Micro-CT scanning using a Quantum GX2 system (PerkinElmer, USA). 3D reconstruction and quantitative analysis were subsequently performed with Mimics Innovation Suite (version 21.0, Materialise, Belgium) and its integrated Analyze 12.0 software. The following microarchitectural parameters were evaluated: bone volume fraction (BV/TV), trabecular thickness (Tb.Th), trabecular number (Tb.N), trabecular separation (Tb.Sp), and bone-implant contact (BIC) ratio.

Postoperative bone specimens were collected at 4 weeks, subjected to graded dehydration and resin embedding, followed by preparation of 5 micrometre-thick hard tissue sections. Histological analysis: sections underwent haematoxylin and eosin (HE) staining, with observation under light microscopy of new bone formation and tissue integration at the bone-implant interface. Immunohistochemical analysis: following dewaxing, sections were incubated overnight at 4 °C with primary antibodies targeting YAP1, Runx2, and OCN, followed by incubation at room temperature for 30 minutes with corresponding secondary antibodies. Sections were then stained with DAB and counterstained with haematoxylin. Positive expression was observed under light microscopy, and the area of positive expression was quantified using Image-Pro Plus software.

The push-out test was employed to evaluate the bond strength at the bone-implant interface: using an Instron 5548 electronic universal testing machine, the maximum load at which the implant separated from the bone tissue was determined at a loading rate of 1 mm min^{-1}. This value served as a quantitative indicator of the interface bond strength.

2.4 Statistical analysis

All data was expressed as mean ± standard deviation and analyzed using SPSS software. Comparisons between multiple groups were performed using one-way analysis of variance, while pairwise comparisons between groups were conducted using LSD-t tests. Differences were considered statistically significant at $P < 0.05$. The statistical significance was denoted as: $^{*}P < 0.05$, $^{**}P < 0.01$, $^{***}P < 0.001$, $^{****}P < 0.0001$; non-significant differences are labeled ns $P > 0.05$.

3 Results

3.1 Coating structure analysis

The surface microstructure, elemental composition, and physicochemical properties of MAO coatings prepared at different voltages were systematically characterized and the results are presented in Fig. 1 and Table 2. SEM morphological observations (Fig. 1a–c) revealed a typical porous micro-nano structure on all MAO coating surfaces, and the discharge pore characteristics exhibited a distinct voltage-dependent trend. With the increase of MAO termination voltage from 400 V to 500 V, the pore size and depth of the coatings increased significantly, and the pore structure evolved from small, uniformly dispersed micropores to a large, interconnected porous network with irregular macropores. The 500 V coating presented the most developed porous structure with the deepest pore depth, which was attributed to the enhanced plasma discharge effect under a higher electric field intensity, leading to more intense sputtering and oxidation on the titanium alloy surface and the formation of a more complex surface topography. The EDS elemental mapping (Fig. 1d–f and Table 2) reveal uniform distribution of O and Ti elements throughout the coating, indicating the formation of a stable TiO_2- based ceramic coating. Ca and P elements were detected in low concentrations in all coatings, derived from the doping of electrolyte ions during the MAO process, and their atomic contents increased slightly with the increase of voltage.

Quantitative analysis of the coating microscopic roughness (Fig. 1g–j) revealed that the surface roughness (R_a) increased in a gradient manner with the increase of voltage: the R_a values of 400 V, 450 V, and 500 V coatings were 9.3 μm, 12.5 μm, and 15.8 μm, respectively. The 3D topographic images of AFM clearly showed that the surface undulation of the coatings was intensified with the increase of voltage, and the 500 V coating presented a more prominent pitted structure, which was consistent with the SEM observation results of the porous structure evolution. Quantitative analysis of coating porosity (Fig. 1l) showed that the porosity was positively correlated with the preparation voltage, increasing from 28.1% (400 V) to 38.6% (500 V). In addition, the coating thickness also exhibited a voltage-dependent increase trend, rising from 10.3 μm (400 V) to 15.6 μm (500 V) (Fig. 1n).

Surface wettability analysis results (Fig. 1m) revealed that the hydrophilicity of the coatings was significantly enhanced with the increase of MAO voltage. The contact angles of 400 V, 450 V and 500 V coatings were 17.4°, 16.8° and 16.3°, respectively. The contact angles of all coatings were close to the superhydrophilic level (<20°), which could effectively promote the subsequent cell adhesion and biological response.

XRD analysis (Fig. 2) revealed that all MAO coatings exhibited characteristic diffraction peaks of anatase and rutile TiO_2. The 500 V coating exhibited a relatively higher rutile phase content, suggesting that elevated voltage enhanced thermal effects and oxygen vacancy formation, thereby facilitating TiO_2 phase transformation.

High-resolution XPS analysis was further used to characterize the chemical bonding states of Ca, P, O elements in the MAO coatings (Fig. 3), to clarify the composition and structural characteristics of the coatings at the molecular level. The Ca 2p spectra of all coatings exhibited a double-peak structure of Ca $2p_3/_2$ and Ca $2p_1/_2$, and the binding energy positions and peak shapes were consistent with the Ca-PO_4 bonding in hydroxyapatite (HA), indicating that the Ca element in the coatings existed in the form of calcium phosphate. The P 2p spectra presented double peaks of P $2p_3/_2$ and P $2p_1/_2$, corresponding to the characteristic peaks of PO_4^{3-}, confirming the presence of phosphate in the coatings. The O 1s spectra could be fitted into three characteristic peaks, which were assigned to Ti–O bonding (TiO_2 matrix), –OH hydrophilic groups and PO_4^{3-} bonding (calcium phosphate), respectively. These results confirmed that the MAO coatings prepared in this study were composite structures composed of TiO_2 ceramic matrix and *in situ* deposited HA.

3.2 Cellular experimental analysis

To evaluate the impact of MAO coatings with varying roughness on cellular behaviour, this study assessed cell proliferation and viability using CCK8 assays and Live/Dead fluorescence staining. CCK-8 assay results (Fig. 4) demonstrated that the OD values of all coatings exhibited an upward trend with increasing incubation time. The proliferation level was positively correlated with coating roughness, with the NC group showing the lowest proliferative activity across all time points for comparison: the OD values of the NC, 400 V, 450 V and 500 V coating groups increased from 0.52, 0.76, 0.85 and 1.06 at day 1 to 1.54, 1.96, 2.37 and 2.65 at day 5, respectively. The 500 V coating group exhibited the most significant proliferative activity, suggesting that higher surface roughness was more conducive to long-term BMSC proliferation.

Live/dead staining results obtained at 48 hours post-seeding showed that the NC group displayed poor cell morphology and

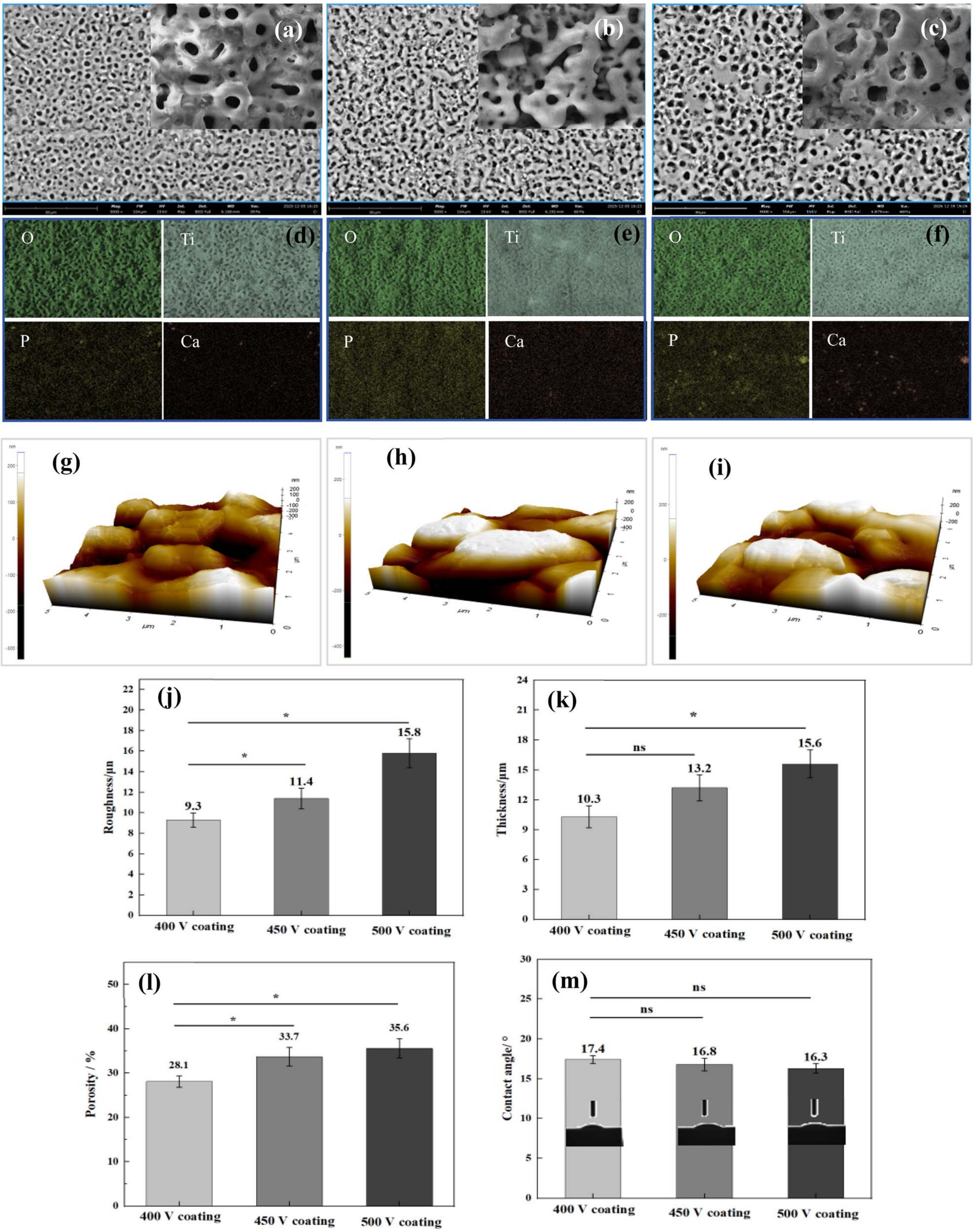

Fig. 1 SEM morphology of different MAO coatings ((a) 400 V, (b) 450 V, (c) 500 V), elemental mapping of O, Ti, P, and Ca for different MAO coatings ((d) 400 V, (e) 450 V, (f) 500 V), AFM topography images corresponding to different MAO coatings ((g) 400 V, (h) 450 V, (i) 500 V), surface roughness values derived from AFM measurements (j), coating thickness (k), coating porosity calculated from SEM images (l), coating contact angle (m), (ns $p > 0.05$, $^{*}P < 0.05$, $^{**}P < 0.01$).

Table 2 Elemental composition (at%) of different MAO coatings

Coatings	Ti	O	Ca	P	Si
400V	36.7	55.9	0.4	1.3	5.3
450V	36.5	55.5	0.5	2.1	5.4
500V	36.4	54.9	0.6	2.2	5.7

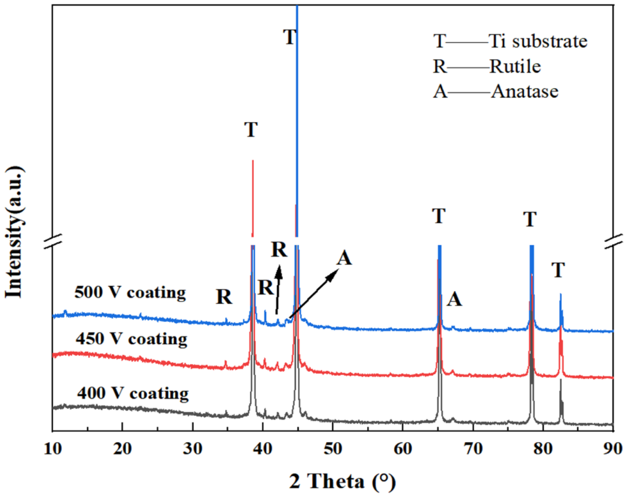

Fig. 2 XRD patterns for different MAO coatings.

low cell density. In contrast, all three MAO coating groups exhibited numerous viable cells labeled with green fluorescence, accompanied by only faint red fluorescent signals indicating dead cells (Fig. 5). No significant differences in cell viability were observed among the three coating groups. This indicated that MAO coatings with varying roughness exhibit favourable cytocompatibility and no obvious cytotoxicity, thus providing a biocompatible interface for cell growth and function.

Rhodamine-phalloidin staining results (Fig. 6) revealed that BMSCs exhibited favourable spreading morphology on the 500 V coating surface, and F-actin filaments displayed dense and orderly arrangement, forming robust and distinct stress fibre bundles. Nevertheless, the F-actin cytoskeleton within cells on the 400 V (Fig. 6) and 450 V coating (Fig. 6) was relatively sparse, exhibiting a lower degree of stress fibre development. Combined with SEM analysis, the porous micro-nano structure and microenvironment with higher surface roughness of the 500 V coating effectively promoted cytoskeletal reorganisation and enhanced adhesion at the cell–material interface.

qPCR assays were performed to quantify the expression of osteogenic genes in BMSCs after 14 days of co-culture with MAO coatings, and the results (Fig. 7a and b) revealed that osteogenic gene expression was upregulated in a porosity- and roughness-dependent manner across all experimental groups. Notably, the 500 V coating group exhibited the most prominent osteogenic induction effect: RUNX2 expression was upregulated to 3.27-fold that of the NC group, corresponding to a 221% increase, while OCN expression reached 6.83-fold that of the NC group (a 499% increase) and was 68% higher than that of the 450 V coating group. RUNX2 acts as a master transcription factor regulating early osteogenic differentiation,[32] and OCN serves as a late-stage marker associated with osteogenic maturation and bone matrix mineralization.[33] The results in Fig. 7c further confirmed that higher porosity and roughness significantly promote the osteogenic differentiation of BMSCs on MAO coating surfaces. The ALP activity of BMSCs increased in a gradient manner with increasing roughness of the MAO coating: The 500 V coating group showed a 76% increase in ALP activity compared to the NC group, and 45.2% and 15.1% higher than the 400 V and 450 V coating groups, respectively.

As a core mechanosensitive transcriptional co-activator of the Hippo pathway, YAP1 activity is dynamically modulated by cytoskeletal tension and extracellular matrix stiffness. Within a stiff ECM, YAP1 undergoes dephosphorylation and nuclear translocation, activating osteogeneic transcriptional programs that direct mesenchymal stem cells toward osteogenic differentiation.[34,35] Analysis of YAP1 expression levels (Fig. 7d) revealed a gradient upregulation with increasing preparation voltage, peaking at 0.47 in the 500 V coating group. These results indicated that the high porosity and micro/nano-scale roughness of the coating enhanced mechanical coupling at the cell–material interface, elevated cytoskeletal tension, and thereby synergistically upregulated the expression of key osteogenic factors.

To investigate the mechanotransduction signaling regulation of BMSCs on different coatings, we analyzed the subcellular localization of the core mechanotranscription factor YAP1 using immunofluorescence staining. BMSCs were cultured on NC, 400 V, 450 V, and 500 V coating groups for 7 days, and the localization of YAP1 was observed (Fig. 8). In the NC group, cells exhibited poor spreading, and YAP1 was mainly distributed in the cytoplasm. With increasing coating porosity and surface roughness, cell spreading was significantly improved, accompanied by progressive nuclear translocation of YAP1. Notably, the 500 V group showed the most extensive cell spreading and the strongest YAP1 nuclear accumulation, indicating that the porous bionic microstructure effectively activates YAP1-mediated mechanotransduction and promotes osteogenic differentiation.

3.3 *In Vivo* safety and bone regeneration analysis

To systematically evaluate the biological safety of the coating samples, HE staining was performed on liver tissue from postoperative SD rats (Fig. 9), with results were analysed in conjunction with the findings of previous *in vitro* cytotoxicity tests. As observed in Fig. 9a, the NC group exhibited a well-defined hepatic lobule architecture, with hepatocytes arranged in regular cords (indicated by red arrows). The central veins maintained intact morphology, hepatocyte nuclei and cytoplasm were uniform in appearance, and no inflammatory cell infiltration was present in the portal areas, that were characteristic features of healthy liver tissue. As shown in Fig. 9b–d for the experimental groups, no significant pathological changes were observed in liver tissue from the 400 V (b), 450 V (c), and

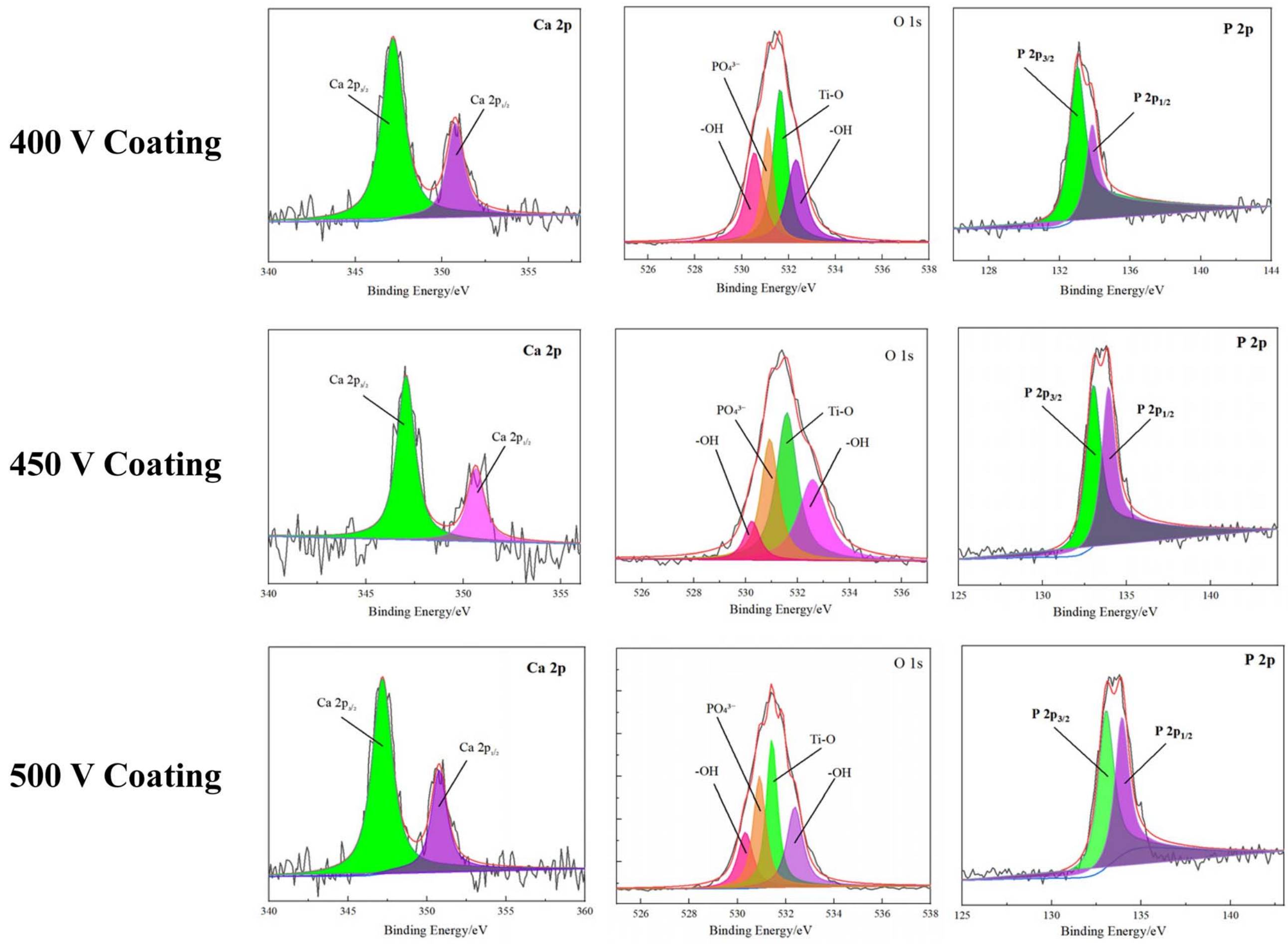

Fig. 3 High resolution XPS spectra of Ca 2p, O 1s, and P 2p for different MAO coatings.

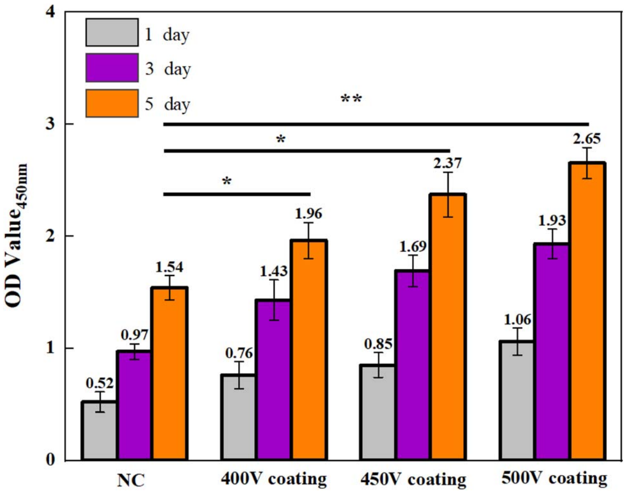

Fig. 4 CCK-8 proliferation assay of BMSCs cultured on different MAO coatings (*$P < 0.05$, **$P < 0.01$).

500 V (d) coating groups. Hepatocyte morphology remained intact with a normal nucleocytoplasmic structure, the hepatic lobule architecture was well preserved, there was no significant inflammatory cell infiltration in the parenchyma or portal areas, no hepatocyte nuclear condensation, fragmentation or eosinophilic necrosis, and no toxicity-related features such as fibrosis or structural disorganisation were detected. The histological characteristics of all experimental groups were highly consistent with those of the NC group, with no statistically significant differences.

Bone regeneration and osseointegration in a rat femoral defect model were assessed by X-ray, micro-CT 3D reconstruction, and quantitative analysis. Fig. 10a shows the femoral defect site, with obvious bleeding at the wound margin, indicating that the surgical procedure was performed in accordance with standard protocols. Fig. 10b and c presents radiographic images taken at 6 weeks post-surgery, clearly delineating the bone defect area and implant position. Surrounding regions exhibit high-density bone formation (yellow circles), indicating new bone formation and mineralisation and confirming favourable osseointegration. The 3D reconstruction in Fig. 10d demonstrates that at 2 weeks post-surgery, all implant groups exhibited limited new bone growth within the coating pores. The 500 V coating group showed more uniform new bone distribution, whereas the NC group exhibited less new bone formation. By week 4, bone regeneration accelerated markedly,

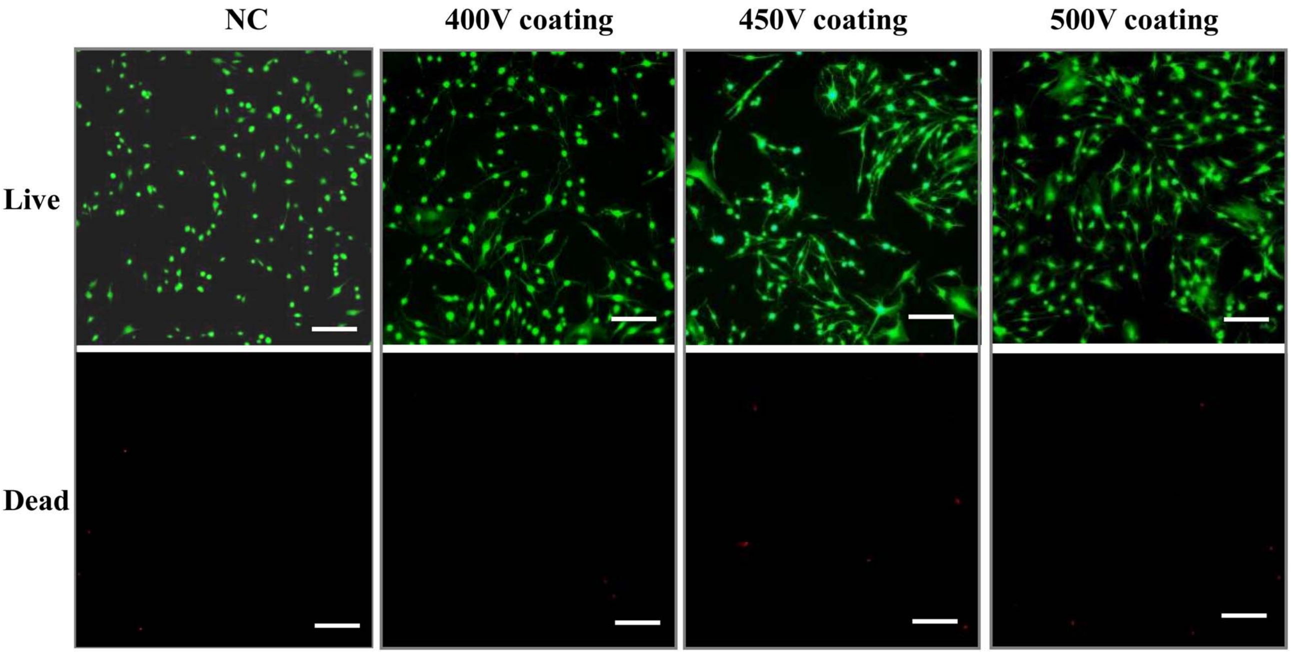

Fig. 5 Live/dead staining of BMSCs cultured on different samples (100×).

with distinct bone bridges forming in the 400 V and 450 V coating groups. The 500 V coating group exhibited the largest bone volume and the most compact structure. By week 6, the 500 V coating group achieved complete fusion at the bone-implant interface with an intact trabecular network, whereas residual unhealed gaps remained in the other groups.

To evaluate the *in vivo* osteogenic performance and osseointegration capability of the porous bionic coatings, the quantitative morphometric parameters are summarized in Fig. 10e–i. The bone volume fraction (BV/TV), a direct indicator of new bone formation at the bone defect site, demonstrated a significant and time-dependent increase in all groups

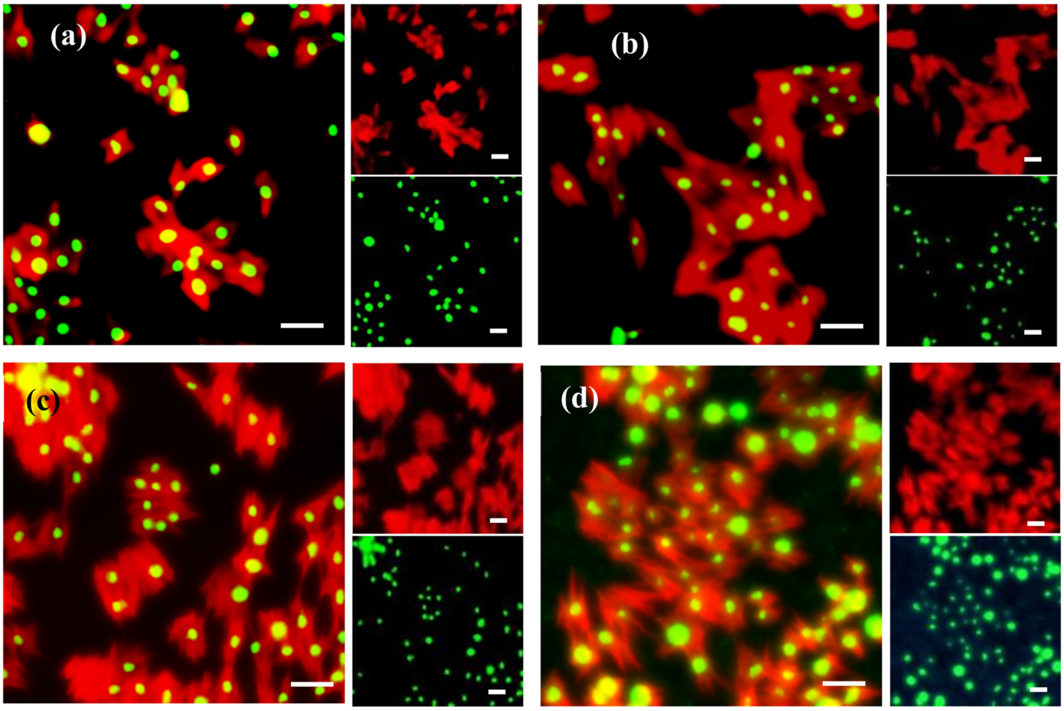

Fig. 6 Rhodamine-phalloidin staining of BMSCs cultured on different samples (400 ×): (a) NC group, (b) 400 V coating, (c) 450 V coating, (d) 500 V coating.

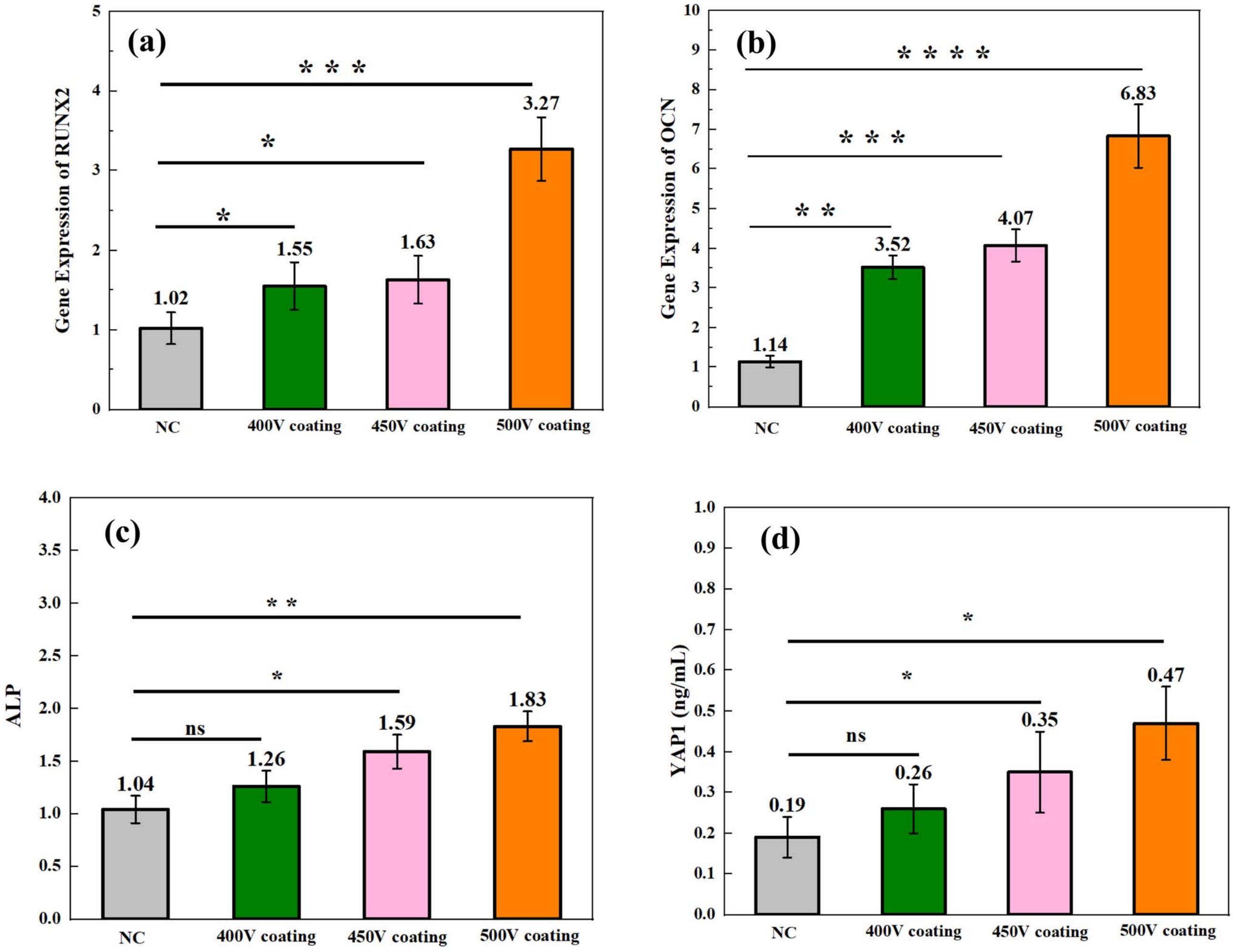

Fig. 7 Osteogenic gene expression following 14 days of co-culture of BMSCs with different samples: (a) RUNX2, (b) OCN, (c) ALP, (d) YAP1. (ns $P > 0.05$, *$P < 0.05$, **$P < 0.01$, ***$P < 0.001$, ****$P < 0.001$).

(Fig. 10e). At the 6 weeks endpoint, the BV/TV for the NC group was ~25.9%. In stark contrast, the implant groups with porous bionic coatings exhibited markedly enhanced bone regeneration, with values of ~28.2% (400 V coating), ~31.8% (450 V coating), and ~33.9% (500 V coating). This corresponds to a 30.9% increase in bone volume for the 500 V coating group compared to the NC group, highlighting its superior osteoinductive potential. The trabecular thickness (Tb.Th) in the 500 V coating group reached approximately 0.29 mm at 6 weeks, representing an 81.3% increase relative to the NC group (approximately 0.16 mm), indicating the formation of a denser and mechanically more functional bone network (Fig. 10f). The bone surface/bone volume ratio (BS/BV) followed a similar trend, with the 500 V coating group showing the highest value (~29.4 mm^{-1} at 6 weeks), reflecting a complex and highly interconnected new bone matrix that was conducive to vascularization and nutrient exchange (Fig. 10g). Concurrently, the trabecular number (Tb.N) was also elevated in the 500 V coating group (~3.5 mm^{-1} *vs.* ~2.6 mm^{-1} for NC group at 6 weeks), indicating a denser trabecular structure (Fig. 10h). The higher Tb.N indicates that the 500 V coating group had greater trabecular density and a more compact microstructure, thereby optimizing stress transfer and improving fatigue resistance. The bone-implant contact ratio (BIC%) is a gold-standard metric for evaluating osseointegration, and the results showed a pronounced improvement in the coating groups (Fig. 10i). By 6 weeks, the BIC% for the NC group reached ~47.3%, whereas the 500 V coating group achieved a significantly higher value of ~68.4%, representing a 44.6% enhancement. The elevated BIC in the 500 V coating group stems from the formation of a HV-enriched oxide layer on its surface. This layer enhanced surface energy and hydrophilicity, facilitating the release of key ions such as Ca^{2+}.

The interfacial bond strength at the bone-implant interface was quantitatively measured by push-out testing at 14, 28, and 42 days post-implantation in a rat femoral defect model. Results (Fig. 11) demonstrated that the interfacial bond strength in all experimental groups increased significantly with implantation time, consistent with the dynamic bone-implant integration process: fibrous tissue formation, new bone deposition, and subsequent mature bone remodeling.[28] Among these, the 500 V coating group demonstrated the most outstanding

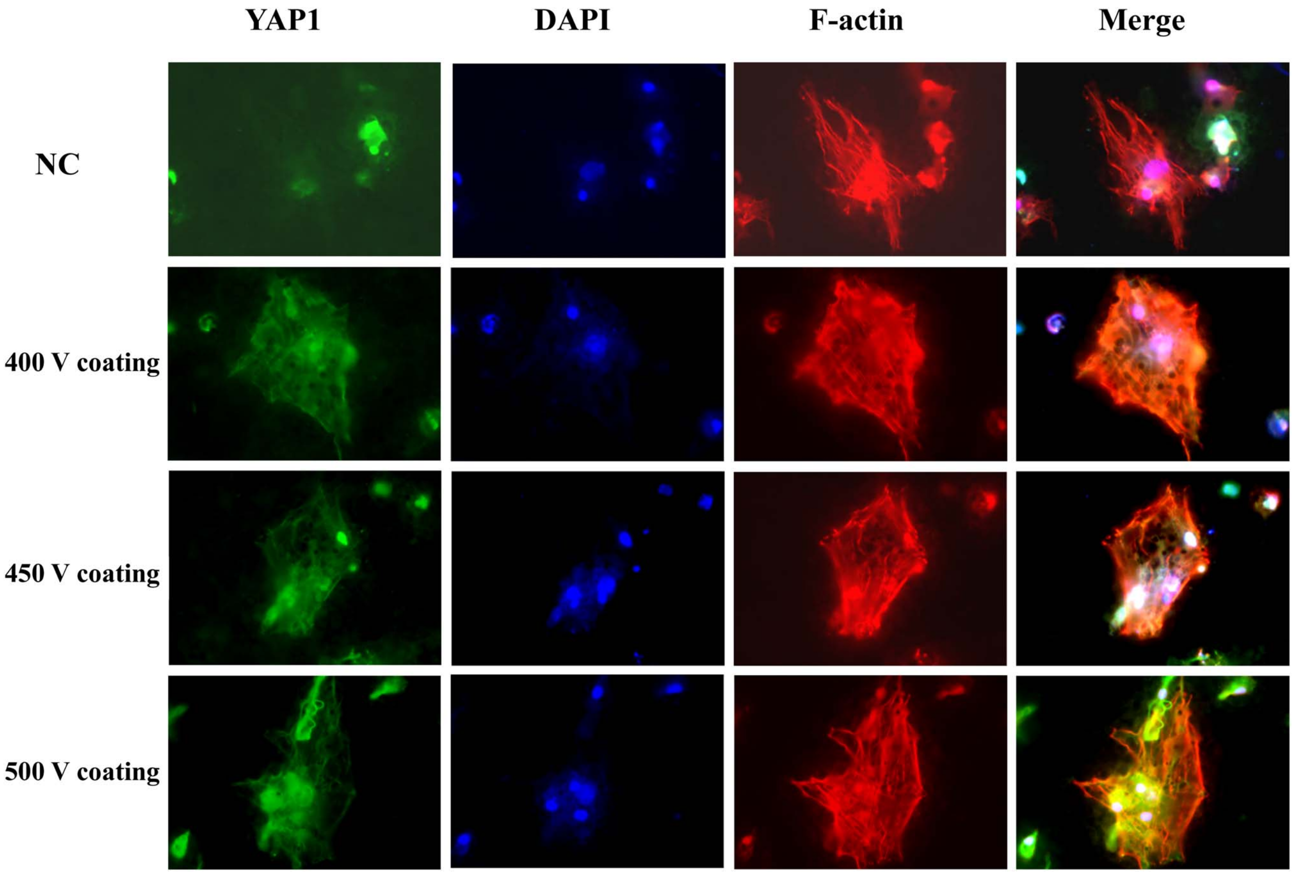

Fig. 8 Immunofluorescence staining of F-actin (red), YAP1 (green), and nuclei (blue) in BMSCs cultured on different samples for 7 days.

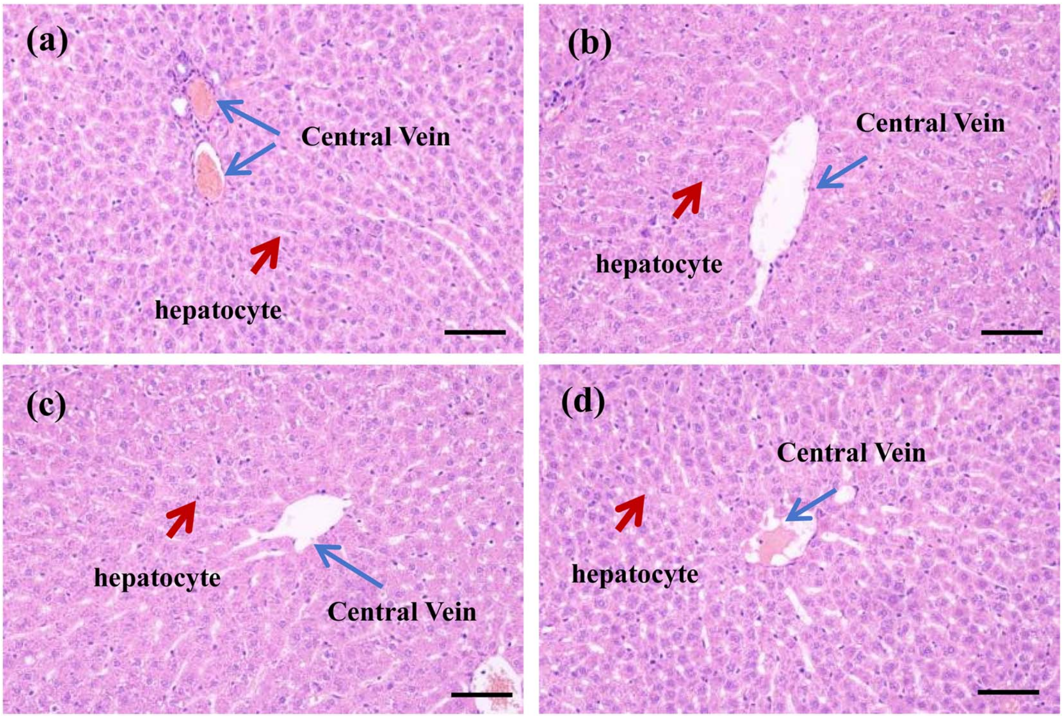

Fig. 9 Hepatic tissue HE staining sections for safety evaluation of different coatings in SD rats (100 ×): (a) NC group, (b) 400 V coating, (c) 450 V coating, (d) 500 V coating.

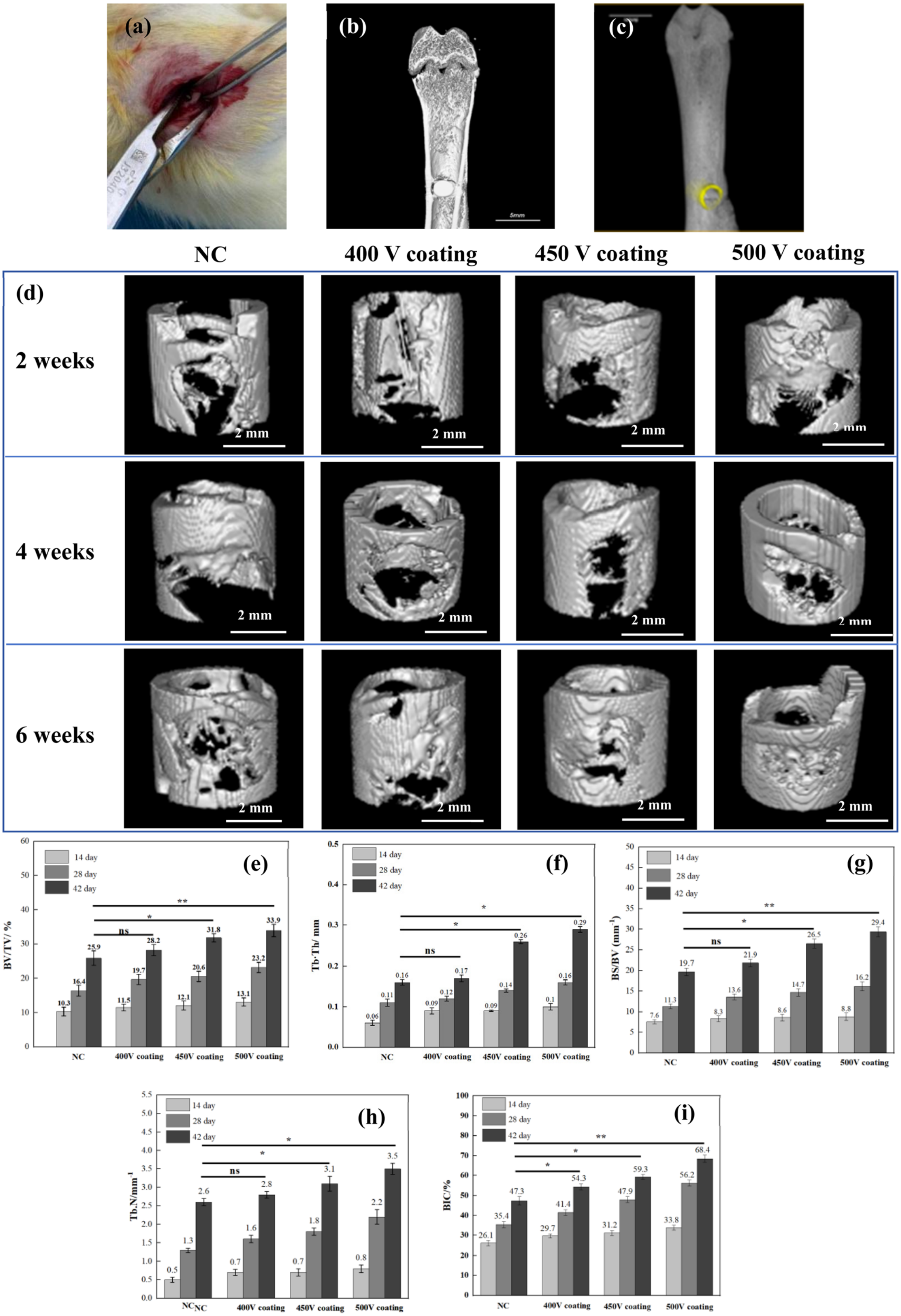

Fig. 10 *In vivo* evaluation of bone regeneration and osseointegration in a rat femoral defect model implanted with different samples using micro-CT and histological analysis. (a) Surgical procedure showing the implantation into the femoral defect site. (b and c) Radiographic images of the femur at 6 weeks post-implantation. (d) 3D micro-CT reconstructions of the femoral defect region at 2, 4, and 6 weeks post-surgery. Quantitative analysis of bone volume fraction (e), trabecular thickness (f), bone surface/bone volume (g), trabecular number (h), bone-implant contact ratio (i). (ns $P > 0.05$, *$P < 0.05$, **$P < 0.01$).

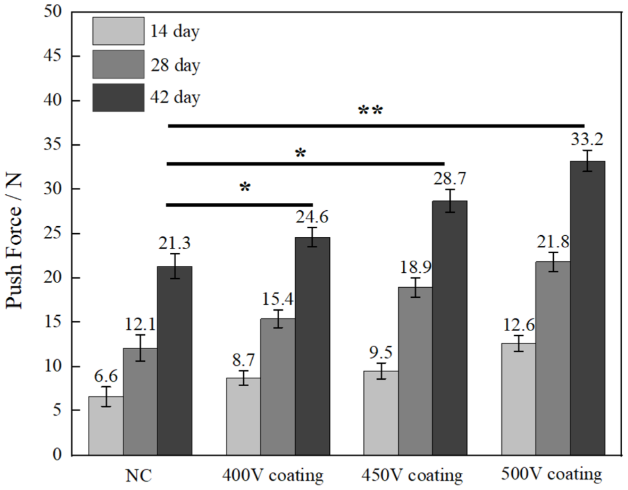

Fig. 11 Dynamic changes in interfacial bonding strength during osseointegration for different samples (*$P < 0.05$, **$P < 0.01$).

performance: at 14 days, the bond strength reached 12.6 N, significantly higher than that of the NC group (6.6 N) and other coating groups; by day 42, it had increased to 33.2 N, representing a 164% rise from baseline and exceeding that of the 450 V coating group (28.7 N), 400 V coating group (24.6 N), and NC group (21.3 N). Crucially, the bond strength increment (11.4 N) in the 500 V coating group between day 28 and 42 was markedly higher than in other groups, suggesting a sustained and enhanced osteogenic effect during the mid-to-late stages of osseointegration. This was primarily attributable to the synergistic effect of coating optimised pore size distribution and the presence of bioactive functional groups (specifically the –OH and $–PO_4^{3-}$ groups contained within hydroxyapatite).

Fig. 12 shows the HE staining of bone tissue and expression analysis of osteogenic differentiation-related proteins (YAP1, RUNX2, OCN) at 4 weeks post-implantation. Grayscale quantitative analysis was performed on the magnified images, as shown in Fig. 12a–c. HE staining results revealed that the bone tissue structure in the NC group remained relatively intact, although new bone formation was minimal. In the experimental group, the area of new bone formation gradually increasing voltage, and was most prominent in the 500 V coating group. This indicated that a higher voltage increased coating porosity, and the three-dimensional pores on the implant surface facilitating bone tissue regeneration.

OCN and RUNX2 protein expression was mainly localized in the bone tissue in the NC group. However, new bone formation around the defect site increased with increasing voltage. Analysis of YAP1- positive signal intensity across groups revealed that the NC group exhibited the lowest expression level, with fewer positive cells and sparse distribution. As the applied voltage increased, the number of YAP1-positive cells increased, and these cells were mainly distributed at the margins of the newly formed bone tissue. Among all groups, the 500 V group demonstrated the strongest YAP1 expression and the highest density of positive cells, which were extensively distributed within bone trabeculae and osteoblast regions. This result indicated that appropriate porosity promotes the osteogenic differentiation of BMSCs, consistent with the findings from *in vitro* experiments.

4 Discussion

This study fabricated different porous micro-nano MAO coatings on titanium alloy by adjusting oxidation voltage (400–500 V), and systematically explored their structure–activity relationship and mechanotransduction mechanism in regulating osteogenic differentiation and osseointegration. Surface characterization confirmed that increased voltage significantly enhanced coating roughness, porosity, thickness and hydrophilicity. The 500 V coating exhibited the most favorable physicochemical properties, with R_a of 15.8 μm, porosity of 38.6%, thickness of 15.6 μm and contact angle close to superhydrophilicity. XRD and XPS verified the coating consisted of TiO_2 matrix and bioactive hydroxyapatite with Ca–P bonding, providing a stable and biomimetic extracellular microenvironment for cell adhesion and osteogenic differentiation.[15]

In vitro cellular experiments demonstrated that all MAO coatings possessed excellent cytocompatibility and no obvious cytotoxicity. Compared with the NC group, BMSCs adhesion, spreading and proliferation were significantly improved on MAO coatings, especially in the 500 V group. The high roughness, interconnected porosity and superhydrophilicity promoted adhesion protein adsorption and provided abundant anchoring sites, facilitating cytoskeletal remodeling and the formation of dense stress fibers.[36] These structural changes strengthened mechanical coupling at the cell–material interface and elevated cytoskeletal tension, which is a prerequisite for mechanotransduction activation.[37]

Osteogenic evaluation revealed that Runx2, OCN and ALP activity were gradually upregulated with increasing coating roughness and porosity, with the 500 V group showing the strongest induction. Higher coating porosity, together with the presence of HA, contributes to enhanced osteogenic differentiation efficiency, which is consistent with previous reports.[38] Immunofluorescence confirmed that high roughness and porosity triggered obvious YAP1 nuclear translocation, while YAP1 expression was significantly elevated and positively correlated with osteogenic differentiation.[39] Nevertheless, this study investigated the underlying molecular mechanisms in the more complex surface environment of MAO coating. These results indicated that the Hippo–YAP1 pathway serves as the core mechanotransduction axis: surface topography elevates cytoskeletal tension, promotes YAP1 dephosphorylation and nuclear accumulation, and further activates the transcription of Runx2 and OCN, ultimately driving BMSC osteogenic differentiation.

In vivo animal experiments validated that MAO coatings, particularly the 500 V group, significantly enhanced bone regeneration, bone-implant contact and interfacial bonding strength. Micro-CT showed markedly increased BV/TV, BMD and trabecular number, while push-out tests confirmed stable interface bonding. Histological observations demonstrated new bone tissue grew into the porous structure and tightly

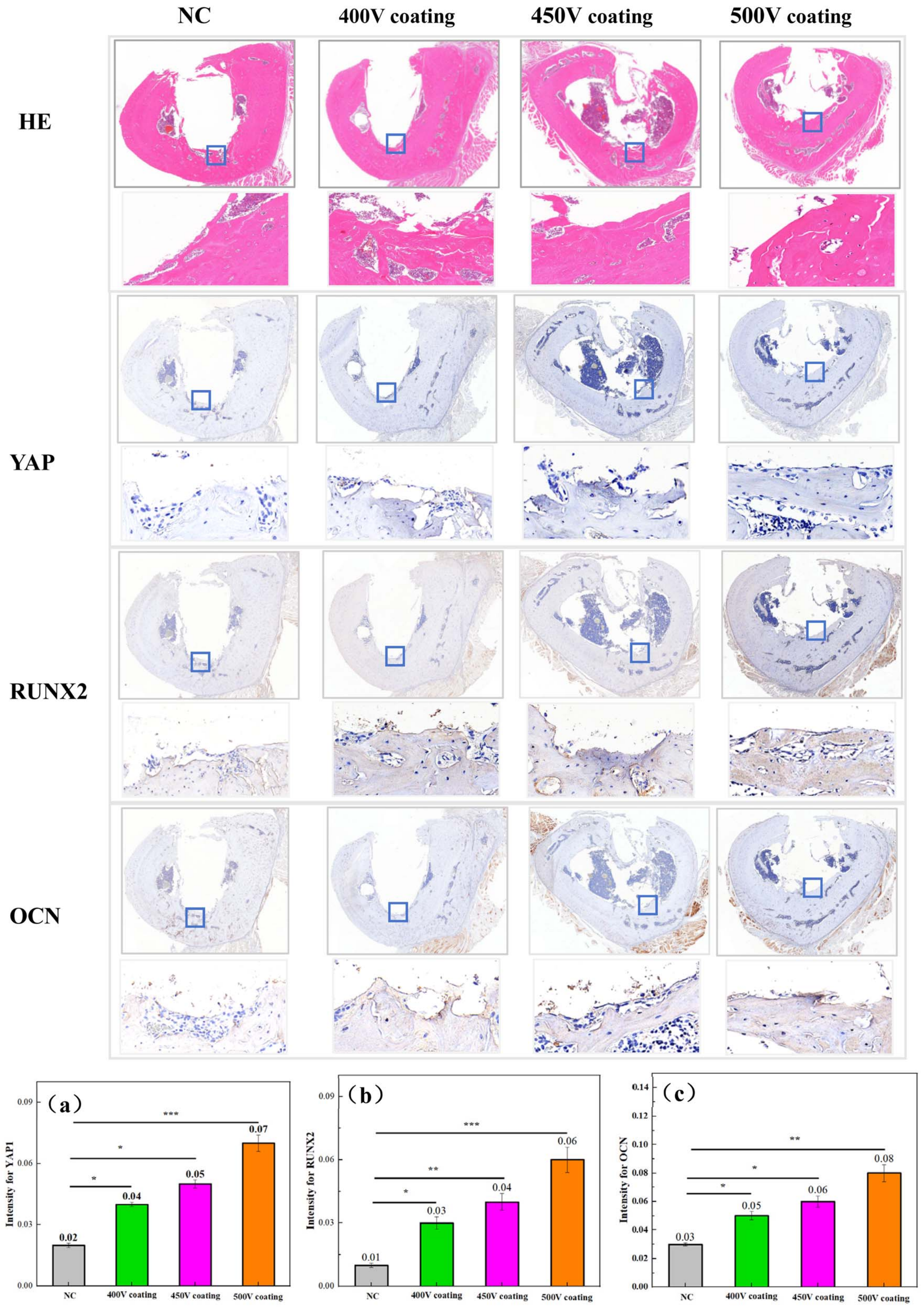

Fig. 12 Histological analysis of bone tissue at 4 weeks post-implantation, HE staining, expression analysis of bone differentiation-related proteins (YAP1, RUNX2, OCN), with quantitative analysis of the mean intensity of YAP1 (a) RUNX2 (b) OCN (c) (*$P < 0.05$, **$P < 0.01$, ***$P < 0.001$).

encapsulated the coating, forming a mechanical interlocking effect.[40] Meanwhile, liver tissue HE staining confirmed good biological safety without systemic toxicity.

In summary, this study revealed that voltage-tunable MAO coatings regulate BMSC fate and osseointegration through the surface topography-cytoskeleton tension-YAP1-osteogenic differentiation axis. The 500 V coating with high roughness, high porosity and bioactive HA composition optimizes the implant microenvironment, effectively promotes bone integration and improves interface mechanical stability, providing a reliable theoretical and experimental basis for surface modification of orthopedic titanium implants.

5 Conclusions

This study elucidated the regulatory mechanisms of MAO coating at the micro-nano scale on cell behavior, osteogenic differentiation, and osseointegration. By modulating MAO voltage, a micro-nano composite porous coating containing HA was constructed, significantly promoting mesenchymal BMSCs spreading with a 35.2% increase in cell area compared to the NC group. At a coating roughness of $R_a = 15.8$ μm, ALP activity increased by 75.96%, while expression of key osteogenic genes Runx2 and OCN was upregulated by 2.25-fold and 4.99-fold, respectively. *In vivo* experiments demonstrated that 4 weeks after implantation into SD rat femurs, the 500 V coating group achieved a BV/TV of 33.9% and a 81.25% increase in Tb.Th. Interface bonding strength reached 33.2 N at 42 days, representing a 55.87% improvement over the NC group. Histology confirmed that new bone tightly enveloped the coating pores, achieving dual reinforcement through bone ingrowth and mechanical anchoring.

Conflicts of interest

The authors declare that they have no conflict of interest.

Data availability

The authors confirm that the data supporting the findings of this study are available within the article.

Acknowledgements

This work was supported by the National Natural Science Foundation of China (52461043), First-class discipline innovation-driven talent program of Guangxi Medical University, 2025 Open Project Funding Program of Guangxi University Engineering Research Center of Advanccd Technologies in Medical and Biological lntelligent Manufacturing, Guangxi(GXGCYJZX2025003), which are gratefully acknowledged.

References

1 J. Humphrey, E. Dufresne and M. Schwartz, Mechanotransduction and extracellular matrix homeostasis, *Nat. Rev. Mol. Cell Biol.*, 2014, **15**(12), 802–812.

2 M. Dalby, A. García and M. Salmeron-Sanchez, Receptor control in mesenchymal stem cell engineering, *Nat. Rev. Mater.*, 2018, 3(3), 1–14.

3 D. Kim, P. Provenzano, C. Smith, *et al.*, Matrix nanotopography as a regulator of cell function, *J. Cell Biol.*, 2012, **197**(3), 351–360.

4 J. Wen, L. Vincent, A. Fuhrmann, *et al.*, Interplay of matrix stiffness and protein tethering in stem cell differentiation, *Nat. Mater.*, 2014, **13**(10), 979–987.

5 J. Wang, X. Chen, R. Li, *et al.*, Standardization and consensus in the development and application of bone organoids, *Theranostics*, 2025, **15**(2), 682–706.

6 J. Zhou, E. Georgas, Y. Su, *et al.*, Evolution from bioinert to bioresorbable: in vivo comparative study of additivelymanufactured metal bone scaffolds, *Adv. Sci.*, 2023, **10**, e2302702.

7 J. Li, H. Fan, L. Hua, *et al.*, Bone implants with triply periodic minimal surface architectures: design, fabrication, and biological performance, *Bio-Des. Manuf.*, 2025, **4**, 8.

8 T. Zhang, Q. Wei and H. Zhou, Sustainable release ofvancomycin from micro-arc oxidised 3D-printed porous Ti6Al4V for treating methicillin-resistant Staphylococcus aureus bone infection and enhancing osteogenesis in a rabbit tibia osteomyelitis model, *Biomater. Sci.*, 2020, **8**, 3106–3115.

9 P. Jin, L. Liu, L. Cheng, *et al.*, Calcium-to-phosphorus releasingratio affects osteoinductivity and osteoconductivity of calcium phosphate bioceramics in bone tissue engineering, *Biomed. Eng.*, 2023, **22**, 12.

10 Q. Chen, Z. Zou, W. Chen, *et al.*, Influence of PRP/GelMA-MAO composite coating on magnesium alloy implants in bone regeneration effect and bio-corrosion properties, *J. Mater. Res. Technol.*, 2025, **36**, 6874–6889.

11 L. Wang, X. You, S. Lotinun, *et al.*, Mechanical sensing protein PIEZO1 regulates bone homeostasis via osteoblast-osteoclast crosstalk, *Nat. Commun.*, 2020, **11**(1), 282.

12 A. Morrell, G. Brown, S. Robinson, *et al.*, Mechanically induced Ca(2p) oscillations in osteocytes release extracellular vesicles and enhance bone formation, *Bone Res.*, 2018, **6**, 6.

13 J. Erben, R. Jirkovec, T. Kalous, *et al.*, Afffliations expand, thecombination of hydrogels with 3D ffbrous scaffolds based on electrospinning andmeltblown technology, *Bioengineering*, 2022, **9**, 660.

14 P. Xiu, Z. Jia, J. Lv, *et al.*, Tailored surface treatment of 3D printed porous Ti6Al4V by microarc oxidation for enhanced osseointegration via optimized bone in-growth patterns and interlocked bone/implant interface, *ACS Appl. Mater. Interfaces*, 2022, **8**, 17964–17975.

15 D. Li, Y. Chen, R. Li, *et al.*, Preparation of biomimetic MAO coating on β-Titanium alloy surface and its bone regeneration property in diabetic environment, *Mater. Des.*, 2024, 239112808.

16 Q. Kun, W. Cheng, Y. Mengmeng, *et al.*, Self-assembly Zn-containing layer on PEO-coated Mg with enhanced corrosion resistance, antibacterial activity, and osteogenic property, *Corros. Sci.*, 2024, **226**, 111674.

17 A. Spyropoulou, K. Karamesinis and E. K. Basdra, Mechanotransduction pathways in bone pathobiology, *Biochim. Biophys. Acta*, 2015, **1852**(9), 1700–1708.

18 C. Zhang, S. Xu, S. Zhang, *et al.*, Ageing characteristics of bone indicated by transcriptomic and exosomal proteomic analysis of cortical bone cells, *J. Orthop. Surg. Res.*, 2019, **14**(1), 129.

19 Q. Zhang, L. Ma, X. Ji, *et al.*, High-Strength Hydroxyapatite Scaffolds with Minimal Surface Macrostructures for Load-Bearing Bone Regeneration, *Adv. Funct. Mater.*, 2022, **32**, 33.

20 Y. Shan, Y. Bai, S. Yang, *et al.*, 3D-printed strontium-incorporated β-TCP bioceramic triply periodic minimal surface scaffolds with simultaneous high porosity, enhanced strength, and excellent bioactivity, *J. Adv. Ceram.*, 2023, **12**(9), 1671–1684.

21 C. Wang, D. Xu, S. Li, *et al.*, Effect of pore size on thephysicochemical properties and osteogenesis of Ti6Al4V porous scaffolds withbionic structure, *ACS Omega*, 2020, **5**, 28684–28692.

22 M. Zhang, T. Gregory and U. Hansen, *at al.*, Effect of stress-shielding-induced boneresorption on glenoid loosening in reverse total shoulder arthroplasty, *J. Orthop. Res.*, 2020, **38**, 1566–1574.

23 M. Hagan, K. Yu, J. Zhu, *et al.*, Decreased pericellular matrix production and selection for enhanced cell membrane repair may impair osteocyte responses to mechanical loading in the aging skeleton, *Aging Cell*, 2020, **19**(1), e13056.

24 M. Lee, D. Lee, J. Jeon, *et al.*, Topographically deffned, biodegradable nanopatterned patches to regulate cell fate and acceleration of bone regeneration, *ACS Appl. Mater. Interfaces*, 2018, **10**(45), 38780–38790.

25 Q. Zhou, O. Castañeda Ocampo, C. Guimarães, *et al.*, Screening platform for cell contact guidance based on inorganic biomaterial micro/nanotopographical gradients, *ACS Appl. Mater. Interfaces*, 2017, **9**(37), 31433–31445.

26 A. Mammoto and D. E. Ingber, Cytoskeletal control of growth and cell fate switching, *Curr. Opin. Cell Biol.*, 2009, **21**(6), 864–870.

27 M. A. Wozniak and C. S. Chen, Mechanotransduction in development: a growing role for contractility, *Nat. Rev. Mol. Cell Biol.*, 2009, **10**(1), 34–43.

28 B. C. Heng, X. Zhang, D. Aubel, *et al.*, Role of YAP/TAZ in Cell Lineage Fate Determination and Related Signaling Pathways, *Front. Cell Dev. Biol.*, 2020, **8**, 735.

29 W. Yang, W. Han, W. He, *et al.*, Surface topography of hydroxyapatite promotes osteogenic differentiation of human bone marrow mesenchymal stem cells, *Mater. Sci. Eng., C*, 2016, **60**, 45–53.

30 Y. Zhang, H. Gong, Y. Sun, Y. Huang and Y. Fan, Enhanced osteogenic differentiation of MC3T3-E1 cells on grid-topographic surface and evidence for involvement of YAP mediator, *J. Biomed. Mater. Res., Part A*, 2016, **104**(5), 1143–1152.

31 J. H. Hwang, D. H. Lee, M. R. Byun, *et al.*, Nanotopological plate stimulates osteogenic differentiation through TAZ activation, *Sci. Rep.*, 2017, **7**(1), 3632.

32 W. Qian, L. Gong, X. Cui, *et al.*, Nanotopographic Regulation of Human Mesenchymal Stem Cell Osteogenesis, *ACS Appl. Mater. Interfaces*, 2017, **9**(48), 41794–41806.

33 E. Arslan, M. Hatip Koc, O. Uysal, *et al.*, Supramolecular peptide nanoffber morphology affects mechanotransduction of stem cells, *Biomacromolecules*, 2017, **18**(10), 3114–3130.

34 X. Wang, X. Hu, I. Dulinska-Molak, *et al.*, Discriminating the independent inffuence of cell adhesion and spreading area on stem cell fate determination using micropatterned surfaces, *Sci. Rep.*, 2016, **6**, 28708.

35 L. Li, S. Yang, L. Xu, *et al.*, Nanotopography on titanium promotes osteogenesis via autophagy-mediated signaling between YAP and beta-catenin, *Acta Biomater.*, 2019, **96**, 674–685.

36 H. Yin, Z. Ruan, T. F. Wan, *et al.*, Metformin ameliorates osteoporosis by enhancing bone angiogenesis via the YAP1/TAZ-HIF1α axis, *Mod. Med.*, 2025, **31**(1), 122.

37 F. Chen, Y. Zhou, Y. Feng and H. Zhu, Study of micro-arc oxidation-polydopamine-nanoclay (MAO-PDA-NC) composite coating on osteogenesis in cranial defect areas of rats, *Dent. Mater. J.*, 2026, **45**(1), 63–71.

38 S. Mv and S. R. Parcha, Porous biocompatible composite scaffold (CS/MFC/HAp) with N-Boc L-cysteine methyl ester for bone tissue engineering applications, *J. Biomater. Sci. Polym. Ed.*, 2025, **36**(18), 2820–2836.

39 J. Luo, M. Walker, Y. Xiao, H. Donnelly, M. J. Dalby and M. Salmeron-Sanchez, The influence of nanotopography on cell behaviour through interactions with the extracellular matrix - A review, *Bioact. Mater.*, 2021, **15**, 145–159.

40 T. Zhang, W. Zhou, W. Yang, *et al.*, Vancomycin-encapsulated hydrogel loaded microarc-oxidized 3D-printed porous Ti6Al4V implant for infected bone defects: Reconstruction, anti-infection, and osseointegration, *Bioact. Mater.*, 2024, **42**, 18–31.